



# Ingenious designed a HER2-Specific macrophage biomimetic multifunctional nanoplatform for enhanced bio-photothermal synergistic therapy in HER2 positive breast cancer

Peng Yang<sup>a,b,1</sup>, Fuyu Du<sup>a,b,1</sup>, Weijie Zhang<sup>a,b</sup>, Weijing Liu<sup>a,b</sup>, Zixuan Ye<sup>a,b</sup>, Hongyu Fan<sup>a,b</sup>, Jie Yu<sup>c</sup>, Karen M. von Deneen<sup>a,b</sup>, Zhongliang Wang<sup>a,b,\*\*</sup>, Pengbo Ning<sup>a,b,\*</sup>

<sup>a</sup> School of Life Science and Technology, Xidian University, Xi'an, Shaanxi, 710071, PR China

<sup>b</sup> Engineering Research Center of Molecular & Neuroimaging, Ministry of Education, Xi'an, Shaanxi, 710071, PR China

<sup>c</sup> Immune Cells and Antibody Engineering Research Center of Guizhou Province, Key Laboratory of Biology and Medical Engineering, Guizhou Medical University, Guiyang, 550025, PR China

## ARTICLE INFO

**Keywords:**  
Biomimetic  
Macrophage  
Anti-HER2  
Breast cancer  
Photothermal therapy

## ABSTRACT

Photothermal therapy (PTT) has garnered extensive attention as an efficient strategy for cancer therapy. Unfortunately, there are currently no suitable photothermal agents (PTAs) capable of effectively treating HER2-positive breast cancer (HER2<sup>+</sup> BC) due to the challenges in addressing blood circulation and tumor accumulation. Here, we propose a HER2-specific macrophage biomimetic nanoplatform IR820@ZIF-8@EM (AMBP) for enhanced bio-photothermal therapy of HER2<sup>+</sup> BC. An anti-HER2 antibody was expressed in engineered macrophages using the transmembrane expression technique. As an efficient PTAs, IR820 dyes were assembled into ZIF-8 as to develop a “nano-thermal-bomb”. Homology modeling methods support that the expressed anti-HER2 antibody can specifically recognize the HER2 receptor. Moreover, antibody-dependent cell-mediated cytotoxicity can also be induced in HER2<sup>+</sup> BC cells by AMBP. *In vitro* fluorescence confocal imaging showed that AMBP promoted the uptake of HER2<sup>+</sup> cancer cells while *in vivo* anti-tumor experiments demonstrated that AMBP efficiently accumulates in the tumor regions. Finally, under spatiotemporally controlled near-infrared (NIR) irradiation, three of the six tumors were eradicated in AMBP-treated mice, demonstrating a safe and effective strategy. In conclusion, our research opens a new paradigm for antibody-specific macrophage, and it is expected that these characteristics will have substantial clinical translation potential for BC treatment.

## 1. Introduction

According to the International Agency for Research on Cancer and the American Cancer Society, breast cancer (BC) make the second leading cause of cancer-related death and the most commonly observed invasive cancer in women [1]. Amplification and/or overexpression of human epidermal growth factor receptor 2 (HER2) occurs in approximately 20 % of all breast cancer cases, which are defined as HER2-positive (HER2<sup>+</sup>) breast cancer; the treatment results for this subtype is unsatisfactory, leading to a poor survival outcome [2]. Adjuvant chemotherapy, such as HER2<sup>+</sup> antibody–drug conjugates (HER2<sup>+</sup> ADCs), is the current mainstay treatment for HER2<sup>+</sup> BC [1,3].

However, drug resistance has emerged as a major cause of treatment failure in patients with HER2<sup>+</sup> BC. Moreover, HER2<sup>+</sup> ADCs drugs can also trigger adverse reactions, such as fatigue, hair loss, hemocytopenia and gastrointestinal disorders; meanwhile, the risk of adverse events increases with the duration and dose of therapy [4]. Herein, this situation calls for innovative modalities to improve or replace existing strategies.

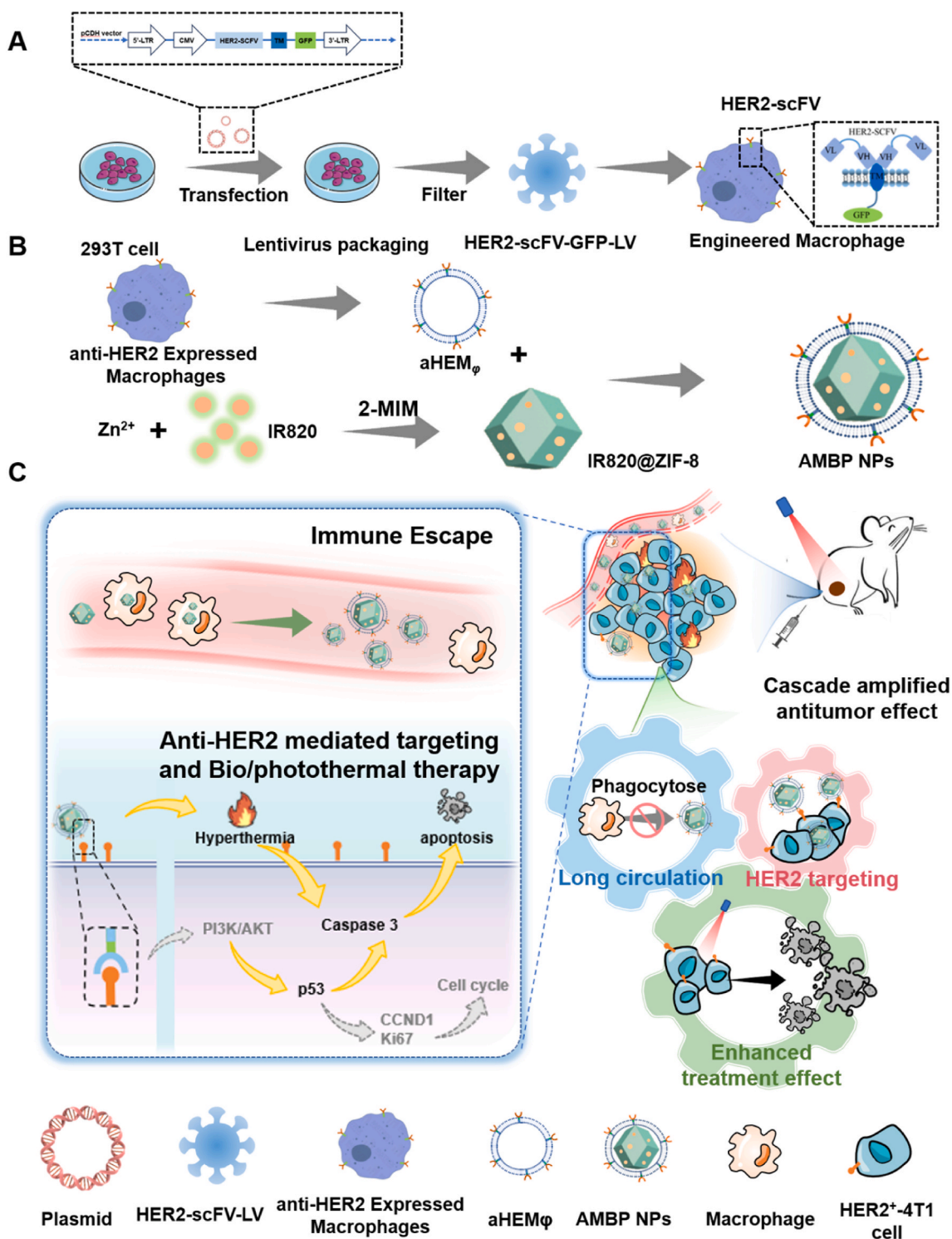
Photothermal therapy (PTT) has garnered extensive attention as a highly efficient tumor ablation therapy with the benefits of spatially tailored photoirradiation, minimal invasiveness, and patient pain relief [5]. Nowadays, nanomaterials have excellent photothermal properties and are often used as photothermal agents (PTAs) in the treatment of BC

\* Corresponding author. School of Life Science and Technology, Xidian University, Xi'an, Shaanxi, 710071, PR China.

\*\* Corresponding author. School of Life Science and Technology, Xidian University, Xi'an, Shaanxi, 710071, PR China.

E-mail addresses: [wangzl@xidian.edu.cn](mailto:wangzl@xidian.edu.cn) (Z. Wang), [pbning@xidian.edu.cn](mailto:pbning@xidian.edu.cn) (P. Ning).

<sup>1</sup> These authors contributed equally to this work.



**Scheme 1.** Illustration of antiHER2 engineered macrophage biomimetic photothermal (AMBP) systems for photothermal/bio therapy of cancer. A) Schematic illustration of anti-HER2 expressed macrophages. The Fabrication of B) AMBP NPs and C) the mechanisms of AMBP NPs-mediated photothermal/bio therapy of cancer.

owing to their ability to efficiently convert light energy into thermal energy [6,7]. Specifically, PTAs accumulate near tumor via intravenous administration or other methods and combine with light source radiation to “burn” tumor cells, resulting in cell necrosis and protein denaturation [7]. For instance, PTT mediated by gold nanoshells has been utilized for high-precision ablation of prostate tumors in clinical trial without causing deleterious effects to organ function [8]. However, PTAs are exogenous materials, and early recognition by the immune

system and clearance by the liver and kidney severely restrict the therapeutically results [9]. On the other hand, local photothermal ablation has certain regional and time limitations [10]. As long as there are residual lesions, there is still the possibility of recurrence and metastasis. To overcome these predicaments, the design and preparation of PTAs are becoming complicated, a lot of functional groups, such as targeting agents, biocompatible components, are modified on PTAs, which is laborious and may increase potential uncontrollable factors.

Biological cell membrane-adorned strategies are intriguing in improving blood circulation and tumor accumulation of PTAs [11,12]. For instance, a series of biological membrane-camouflaged nanoparticles with extended half-lives were created by Zhang and his collaborators [13–15]. In terms of tumor accumulation, the modification of tumor-targeting agents (e.g., aptamers, peptides, and antibodies) on membrane could enhance the recognition of the overexpressed surface antigens of cancer cells based on ligand-receptor interaction [16]. Direct surface modification by adsorption or covalent binding can be delivered at tumor targeting performances. However, low coupling efficiency and randomly oriented antibodies by above methods results in a low specificity and affinity, besides low yield, of anti-body [4]. Our lab recently successfully created urokinase-type plasminogen activator (uPA) scavenger-armed macrophages by gene engineering method, which demonstrated extracellular expressed proteins performed superior biological activity, and have a significant anti-metastatic effect on the 4T1-tumor [17]. As a top-down approach, the antibody-specific biomimetic PTAs bypass the laborious group-modified engineering. Owing to the reserved antigens and cell membrane structure, antibody-specific biomimetic PTAs can acquire special functions, such as ligand recognition and targeting, long blood circulation, and immune escaping, offering a promising PTA for photothermal therapy. Therefore, we hypothesized that rational construction of macrophages and antiHER2 within a PTA nanoplatform could not only achieve a properly oriented antibody for high specificity to HER2<sup>+</sup> BC tumor, but also improve their blood circulation time and tumor accumulation result. However, to the best of our knowledge, the paucity of reports is on developing multifunctional HER2-specific macrophage biomimetic nanoplatforms, which is very important to the blossom of PTT for HER2<sup>+</sup> BC therapy.

Herein, we developed a multifunctional HER2-specific macrophage biomimetic nanoplatform to provide inherent tumor enrichment tropism and intrinsic biotherapy functionality for effective targeting and potent treatment of tumors. Anti-HER2 engineered macrophages (EM) were created by first developing and then extracting anti-HER2 macrophages, as indicated in Scheme 1. Due to the controlled and significant therapeutic effects of photothermal therapy, IR820 dyes and ZIF-8 nanocarriers were used as neoadjuvant tools to create a "nano-bomb" that has synergistic anti-tumor effects *in vitro* and *in vivo*. After being administered to HER2<sup>+</sup> BC tumor-bearing mice, anti-HER2 engineered macrophage biomimetic photothermal nanoparticles (IR820@ZIF-8@EM named as AMBP NPs) escaped from the reticular macrophage system and actively target HER2 expressed 4T1 tumor cells, leading to increased accumulation in tumors with minimal systemic toxicity. Moreover, due to the properties of IR820 dyes, they could then, under continuous 808 nm laser irradiation, convert light energy into heat energy and cause local hyperthermia that may destroy tumor cells and enhance the anti-tumor benefits of biotherapy. Furthermore, antibody-dependent cell-mediated cytotoxicity can also be induced in HER2<sup>+</sup> BC cells by AMBP NPs because antibody (HER2 scFV) is produced on the surface of macrophages [18]. In summary, fluorescence imaging is used to guide the implementation of synergistic photothermal therapy and biotherapy, indicating the desired anti-tumor efficacy. In addition to the aforementioned advantages, these strategies can be extended to other antibodies and treatments, such as PD-L1 chemotherapy or radiotherapy. It is expected that these characteristics will have substantial clinical translation potential for BC treatment.

## 2. Materials and methods

### 2.1. Materials

2-Methylimidazole, Zinc acetate, IR820 and Rh6G were obtained from Sigma Company (St. Louis, USA). 3T3, 293T, RAW264.7, 4T1, and SKOV3 cell lines were obtained from the Chinese Academy of Sciences Cell Bank. 3-[4,5-dimethylthiazol-2-yl]-2,5-diphenyltetrazoliumbromide (MTT), 4',6-diamidino-2-phenylindole (DAPI), Dulbecco's

modified eagle's medium (DMEM) and fetal bovine serum (FBS) were purchased from Gibco Corp. Calcein acetoxymethyl ester (Calcein AM) and propidium iodide (PI) were attained from Beyotime. All reagents were analytical reagents (A.R.) and directly used if without special instructions.

### 2.2. One-pot synthesis of IR820@ZIF-8 nanoparticles

IR820@ZIF-8 nanoparticles were prepared by one-pot synthesis method. First, 624 mg 2-MIM were dissolved in 2.4 mL solution, and 0.5 mL IR820 solution (2 μg/μL) was prepared as the original solution, respectively. Then, 0.4 μL zinc acetate solution (40 mg) was added into the mixture. After stirring vigorously for 1 h at 40 °C, the synthesized IR820@ZIF-8 NPs were separated by concentration at 12000 rpm for 15 min and then washed three times with deionized (DI) water and re-dispersed in DI for further use.

### 2.3. Preparation of antiHER2 engineered macrophage membrane

In brief, we transform a plasmid DNA encoding HER2-scFV sequence into 293T cell lines to obtain HER2-scFV-LV. The plasmids HER2-scFV, Rev, Gag and VSV were added to Opti-MEM and incubated for 5 min. TurboFect Transfection Reagent and pipet were mixed and then incubated for 15–20 min. Above incubated mixture were added to the 6-well plate of 293T cells, The cell culture plate was reset to 37 °C and 5 % CO<sub>2</sub> and cultured for 48 h. Centrifuge the cell culture obtained in the above steps at 3000 rpm for 5 min in a centrifuge tube, and next the supernatant was transferred to a new sterile centrifuge tube for the next step of purification. Finally the culture containing lentivirus were centrifuged for future use. Then, with the infection of RAW264.7 macrophages with HER2-scFV-LV, the anti-HER2 expressed RAW264.7 macrophages are constructed. The successful construction of antiHER2 engineered macrophages are verified by CLSM imaging, and mRNA level expression by RT-qPCR.

### 2.4. Preparation of AMBP nanoparticle

The antiHER2-engineered macrophage (named as "aHEM<sub>φ</sub>") cell membrane was first extracted and obtained. Briefly, aHEM<sub>φ</sub> was digested, collected, and dispersed in ultrapure water, and further lysed via repeated freezing and thawing for several times. Subsequently, the achieved aHEM<sub>φ</sub> was separated by centrifugation at 3000 rpm for 15 min at 4 °C to remove the sediment, and the supernatant was further centrifuged at 12000 rpm for 30 min at 4 °C to obtain the cell membrane, which was re-dispersed in ultrapure water for further use.

To synthesize the aHEM<sub>φ</sub> cell membrane coated IR820@ZIF-8 NPs, aHEM<sub>φ</sub> (20 mg) placed in DI water (2 mL) was injected into IR820@ZIF-8 NPs dispersion (10 mg within 5 mL), and then the mixed solution was under sonication (50 W) until it was clear and transparent. Finally, the mixture of NPs was centrifuged at 12000 rpm for 10 min, followed by several washes with DI water. The aHEM<sub>φ</sub> cell membrane coating was then visualized by SDS-PAGE and SEM.

### 2.5. Macrophage cell membrane protein characterization

The engineered macrophage cell membrane of AMBP NPs were visualized by the sodium dodecyl sulfate-polyacrylamide gel electrophoresis (SDS-PAGE) method. The proteins were extracted from the macrophages (M<sub>φ</sub>), and aHEM<sub>φ</sub>, IR820@ZIF-8@M<sub>φ</sub> (MBP NPs) and AMBP NPs via repeated freezing. After quantification by the BCA assay kit, equal protein contents (100 μg) of the samples were loaded onto the wells of the 10 % SDS-PAGE gel. After electrophoresis, the protein bands were stained with Coomassie blue for 2.5 h and de-stained for 30 min before photographing.

## 2.6. Photothermal effects of AMBP NPs

To evaluate the photothermal effects of AMBP NPs, AMBP NPs dispersion was irradiated by an 808 nm near-infrared (NIR) laser. Different kinds of AMBP NPs dispersions (0, 10, 25, 50, 100  $\mu\text{g mL}^{-1}$ ) were placed in a 96-well plate, with an 808 nm NIR laser (0.25, 0.5, 1  $\text{W cm}^{-2}$ ) and illuminated for 5 min; the temperature rise was recorded through the infrared thermal camera (InfraTec, Germany). To calculate the photothermal conversion efficiency, the absorption spectra of AMBP NPs at 100  $\mu\text{g mL}^{-1}$  were detected using an ultraviolet-visible (UV-Vis) spectrophotometer. And the detailed calculation was given as following [19]:

$$\eta = \frac{hs\Delta T_{max} - Q_s}{I(1 - 10^{-A_{808}})}$$

$$\tau = \frac{m_s C_s}{hS}$$

where  $h$  is the heat transfer coefficient,  $S$  is the surface area of the container,  $\Delta T_{max}$  is the temperature change of the nanoparticle suspensions at the maximum steady state temperature.  $Q_s$  is the heat associated with the NIR-light absorbance of the solvent.  $I$  is incident laser density (1  $\text{W cm}^{-2}$ ), and  $A_{808}$  is the absorbance of the nanoparticles at 808 nm. where  $\tau$  is the sample system time constant,  $m_s$  and  $C_s$  are the mass and the heat capacity of the solvent (pure water), respectively.

## 2.7. Cytotoxicity assay

3T3, 4T1, and SKOV3 cells lines were selected to assess the cell cytotoxicity. In short, 4T1 and SKOV3 cells were incubated in 96-well plates for 24 h for attachment. Then, different recipes of nanoparticles aqueous dispersions were added in and co-incubated for 24 h. Finally, the cell viability was measured with a standard MTT assay.

## 2.8. Cellular uptake of AMBR NPs

To investigate cellular uptake behaviors of different kinds of nanoparticles by cells, HER2<sup>+</sup>-4T1 and SKOV3 cancer cells were seeded into 24-well plates and cultured in the incubator overnight. Then, Free Rh6G, 100  $\mu\text{g mL}^{-1}$  Rh6G@ZIF-8, MBR, and AMBR were added and cultured with cells for 2 h. Thereafter, the treated cells were gently washed with fresh PBS, and stained with DAPI (10  $\mu\text{g mL}^{-1}$ ) for 15 min. The cellular uptake behaviors in HER2<sup>+</sup>-4T1 and SKOV3 were imaged with CLSM.

## 2.9. Flow cytometry analysis

To investigate cellular uptake behaviors of different kinds of nanoparticles by cells, HER2<sup>+</sup>-4T1 and SKOV3 cancer cells were seeded into 6-well plates and cultured in the incubator overnight. Then, Free Rh6G, 100  $\mu\text{g mL}^{-1}$  Rh6G@ZIF-8, MBR, and AMBR were added and cultured with cells for 2 h. Thereafter, the treated cells were gently washed with fresh PBS, and the cellular uptake behaviors in HER2<sup>+</sup>-4T1 and SKOV3 were obtained by the BD flow cytometry system.

## 2.10. In vitro PTT assay

HER2<sup>+</sup>-4T1 was seeded in 96-well plates for 24 h incubation, and the cells were treated with the different recipes of nanoparticle aqueous dispersions for 6 h to allow cellular uptake. Then, the cells in each plate were irradiated with an NIR laser (808 nm, 1  $\text{W cm}^{-2}$ , 5 min). After 24 h incubation, standard MTT assay, and live/dead cell viability assay were used to measure the viability of cells.

## 2.11. Anti-cellular uptake of macrophages

To investigate cellular uptake behaviors of different kinds of nanoparticles by macrophages, free Rh6G, 100  $\mu\text{g mL}^{-1}$  Rh6G@ZIF-8, MBR, and AMBR were added and cultured with cells for 2 h. Thereafter, the treated cells were gently washed with fresh PBS, and stained with DAPI (10  $\mu\text{g mL}^{-1}$ ) for 15 min. The cellular uptake behaviors in macrophages were imaged with CLSM.

## 2.12. RT-qPCR assay

RNA extraction and quantitative real-time PCR Total RNA was extracted using TRIzol universal reagent (TIANGEN Biotech Co., Ltd., Beijing, China) according to the manufacturer's protocol. The expressions of P53, CCND1, Caspase-3, Ki67, AKT, PI3K, and GAPDH in cancer cells after different treatments were assessed using RT-qPCR. In the process of standardizing RT-qPCR results, standard normalization is performed using the 2<sup>- $\Delta\Delta\text{Ct}$</sup>  formula.

## 2.13. Construction of HER2<sup>+</sup>-4T tumor-bearing mouse

Animal experiment ethics approval was approved by the Institutional Animal Care and Use Committee of the Fourth Military Medical University (approval number: 20200316). Female 6-week-old BALB/c mice (B&K Laboratory Animal Co., Ltd., Shanghai, China) were housed under standard breeding conditions and provided with plenty of food and water. After 7 days, approximately  $6 \times 10^5$  HER2<sup>+</sup>-4T1 cells in 100  $\mu\text{L}$  PBS were subcutaneously injected into the right flank of each mouse. After two weeks, when tumors reached  $\sim 50\text{--}80 \text{ mm}^3$ , the HER2<sup>+</sup>-4T1 tumor-bearing mice were randomly assigned for treatment. The volume of the tumor was calculated by the following formula:  $V(\text{mm}^3) = (\text{width of tumor})^2 \times \text{length of tumor} / 2$ .

## 2.14. In vivo fluorescence imaging, tissue distribution, and pharmacokinetics

To evaluate the biodistribution of AMBP and its pharmacokinetics. HER2<sup>+</sup>-4T1 tumor-bearing was established, once the tumor volume reached 100  $\text{mm}^3$ , and different recipes of nanoparticles were intravenously injected for imaging research. At the predetermined time (0, 2, 4, 6, 8, 10, 12, 24, 48 h) after injection, the *in vivo* tumor imaging was monitored.

For pharmacokinetics study, twelve BALB/c mice (female, 20–22 g) were randomly divided into three groups: IR820@ZIF-8, MBP, and AMBP group, in which mice received 100  $\mu\text{L}$  of nanoparticles (2  $\text{mg/mL}$ ) intravenously, respectively. At different time points post injection (i.e. 1, 2, 4, 6, 8 and 24 h), 100  $\mu\text{L}$  of blood were collected from mouse orbit and diluted to 1000  $\mu\text{L}$  with PBS buffer (10 mM, pH = 7.4). The blood samples were centrifuged at 1200 rpm for 5 min, and the supernatant were collected for fluorescence intensity measurement (Ex: 710 nm, Em: 820 nm).

## 2.15. In vivo phototherapy

HER2<sup>+</sup>-4T1 tumor-bearing mice were divided into five groups, and each group had six mice: group 1: PBS; group 2: IR820@ZIF-8 with laser irradiation; group 3: ZIF-8@EM $\phi$ ; group 4: MBP NPs with laser irradiation; and group 5: AMBP NPs with laser irradiation. Each group of mice was administered with different nanomaterials (100  $\mu\text{L}$ , 2  $\text{mg mL}^{-1}$ ) via tail vein and then irradiated with 808 nm NIR laser (1  $\text{W cm}^{-2}$ ) for 5 min at 8 h post-injection. The procedures for the tumor treatment were described in our previously reported protocol [20].

## 2.16. Statistical analysis

Results in this paper are given as mean result  $\pm$  SD (standard

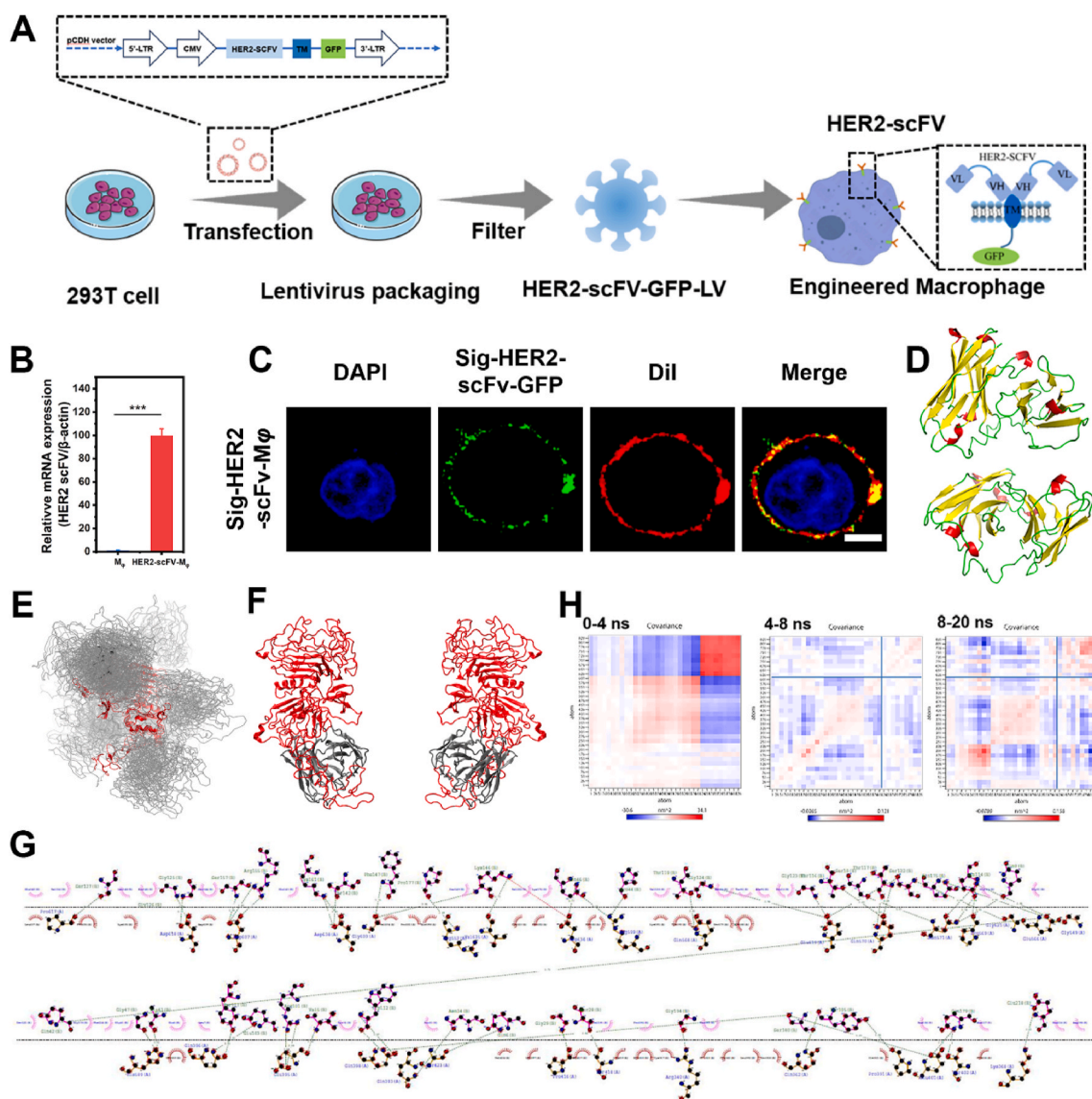


**Fig. 1.** Construction of anti-HER2 expressed macrophages. A) Schematic illustration of anti-HER2 expressed macrophages. B) The mRNA expression level of HER2-scFV-macrophages. C) CLSM results of HER2-scFV-GFP-macrophages with DiI to verify their transmembrane expression. HER-2-scFV-GFP were presented with green, macrophage was labeled with DiI (Red), and nuclei were stained with DAPI (Blue). D) The Structure of the anti-HER2 protein domain. E) The Binding areas determined from molecular docking of HER2 (red region) and anti-HER2 (gray region). F) The Binding results obtained by molecular dynamic simulation in this work. G) The Residue interaction between HER2 and anti-HER2 obtained by molecular dynamic simulation. H) Cross-correlation matrices of the coordinates' fluctuations for C $\alpha$  atoms around their mean positions during the equilibrium simulation. Red color represents correlated motions and blue color represents anti-correlated motions. Results are presented as means  $\pm$  SD. \*\*\* $P < 0.001$ .

deviation). Two-way analysis of variance (ANOVA) with a post-hoc test (Bonferroni's multiple-comparison test) was used to compare and assess statistical significance among all groups. \* $P < 0.05$ , \*\* $P < 0.01$ , and \*\*\* $P < 0.001$  indicated statistical difference.

### 3. Results and discussion

#### 3.1. Preparation and biochemical property characterization of Anti-HER2 EM

The accumulation of drugs directly affects therapeutic results [21]. We initially built an anti-HER2 modified macrophage membrane to accelerate blood circulation and tumor accumulation. For producing HER2-scFV-LV, 293T cells were transfected with a plasmid encoding the HER2-scFV sequence. Next, anti-HER2 expressing macrophages were generated by transfecting macrophages with HER2-scFV-LV (Scheme 1A

and Fig. 1A). Anti-HER2 transmembrane expression maintained the same cell size and vitality as typical macrophages (Fig. S1). RT-qPCR was performed to determine the mRNA expression of the HER2-scFV sequence (Fig. 1B). Based on the transmembrane features of designed HER2-scFV, we designed a GFP linked with HER2-scFV as a marker to indicate the expressing of HER2-scFV (Fig. 1C). After incubation, the membrane dye DiI (red fluorescence) was used for staining. HER2-scFV-GFP proteins were produced on 293T cells and macrophages, as shown by the green fluorescence signal in Fig. 1C, which colocalized well with DiI dyes (Fig. S2). These findings demonstrate that the HER2-scFV protein is expressed via the membrane.

Then, we evaluated whether the transmembrane expression of HER2-scFV could inherit its recognition ability because of the significance of HER2 antibody orientation in the antigen-antibody recognition for biotherapy. By homology modeling techniques, the anti-HER2 protein domain's 3D dimeric structure was created (Fig. 1D and Fig. S3)

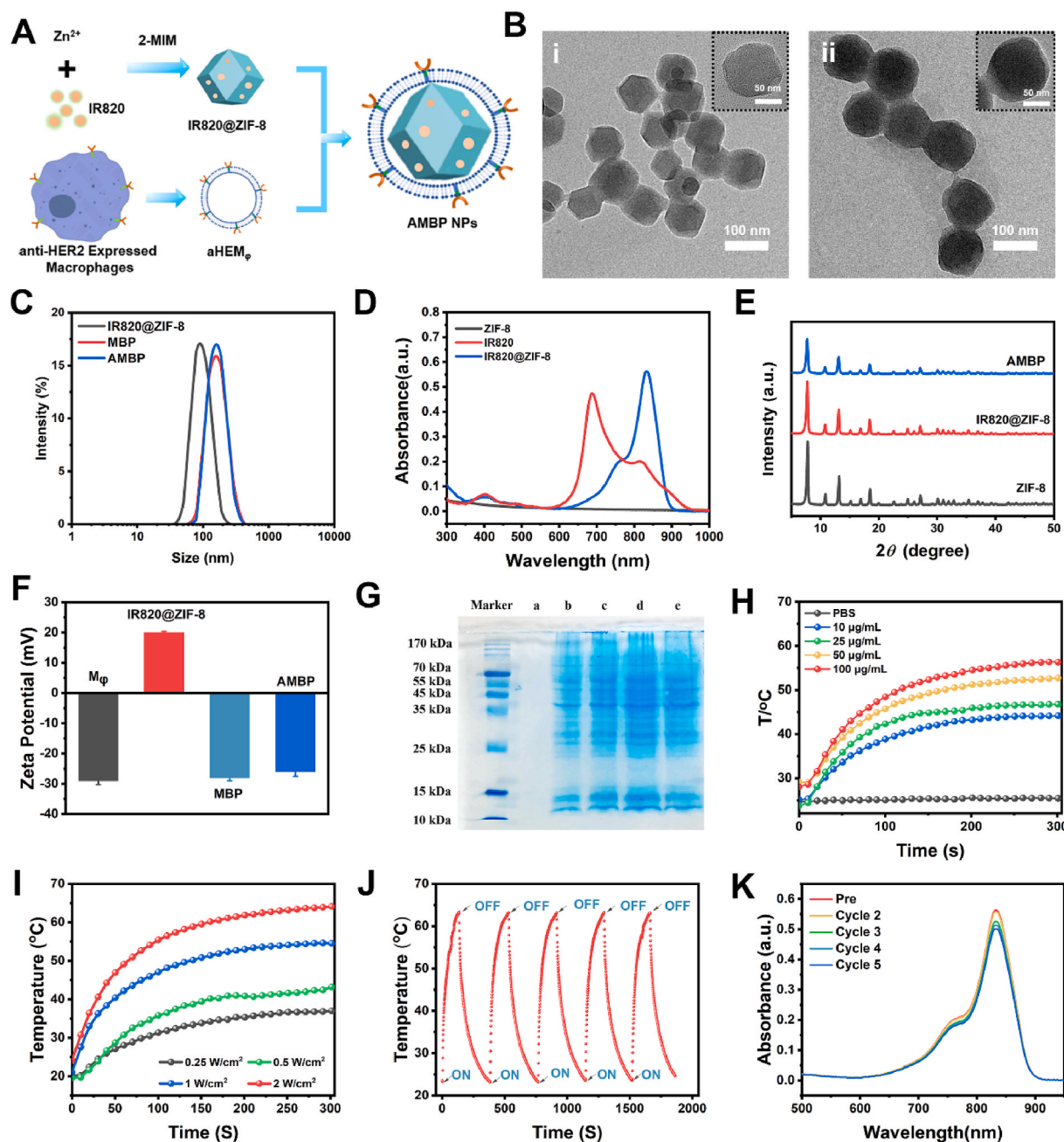


**Fig. 2.** Preparation and characterization of Biomimetic-Nano-Bio systems with phototherapeutic payload. A) Scheme to construct AMBP nanoplatform. B) Transmission electron microscope (TEM) data to show the morphology of IR820@ZIF-8 and AMBP, and the inserted pictures display the clearer morphology of AMBP. C) DLS data of IR820@ZIF-8, MBP and AMBP. D) UV-vis spectra of ZIF-8, IR820, and IR820@ZIF-8. E) X-ray diffraction spectra of ZIF-8, IR820@ZIF-8, and AMBP. F) Zeta potential results of different formats within AMBP to verify their successful coating. G) SDS-PAGE protein analysis, a: ZIF-8 nanomaterials, b: Macrophages, c: MBP NPs, d: aHEM<sub>p</sub>, e: AMBP NPs. H) Photothermal effects of AMBP NPs with different concentrations. I) Photothermal effects of AMBP NPs with different laser power. J) Photostability of AMBP dispersed solution after five “ON-OFF” cycles. K) Absorbance change of AMBP dispersed solution after five “ON-OFF” cycles.

[22]. Meanwhile, a protein docking analysis was conducted to investigate the probable binding sites between HER2 and anti-HER2 with the help of the HDock server [23]. To identify the underlying binding sites of anti-HER2 on the skeleton of HER2, 100 docking conformations with the lowest binding affinities were collected and depicted using the open-source PyMOL (Molecular Graphics System, Version 2.6.0a0. Schrodinger, LLC). The four key binding sites of HER2 that interact with the anti-HER2 protein are indicated in Fig. 1E, where these areas around the HER2 protein exhibit a large distribution of anti-HER2 conformations. The docking area in Fig. 1E corresponds to extracellular domain IV of HER2, according to the molecular dynamics’ simulations in Fig. 1F.

The investigation of the amino acid residue interactions between HER2 and anti-HER2 demonstrated high-affinity interactions, such as hydrogen bond contact, van der Waals forces, and hydrophobic-hydrophobic interactions (Fig. 1G) [24]. Finally, the migration of C atoms throughout the binding process was confirmed using the cross-correlation matrices of the coordinate fluctuations around their mean positions. Regions of extremely positive movement are depicted in red, and regions of strongly negative movement are depicted in blue in Fig. 1H [25]. Fig. 1H shows the correlated motion of HER2 and anti-HER2 protein residues dispersed throughout different locations during the first equilibrium stage. Unsurprisingly, the residues

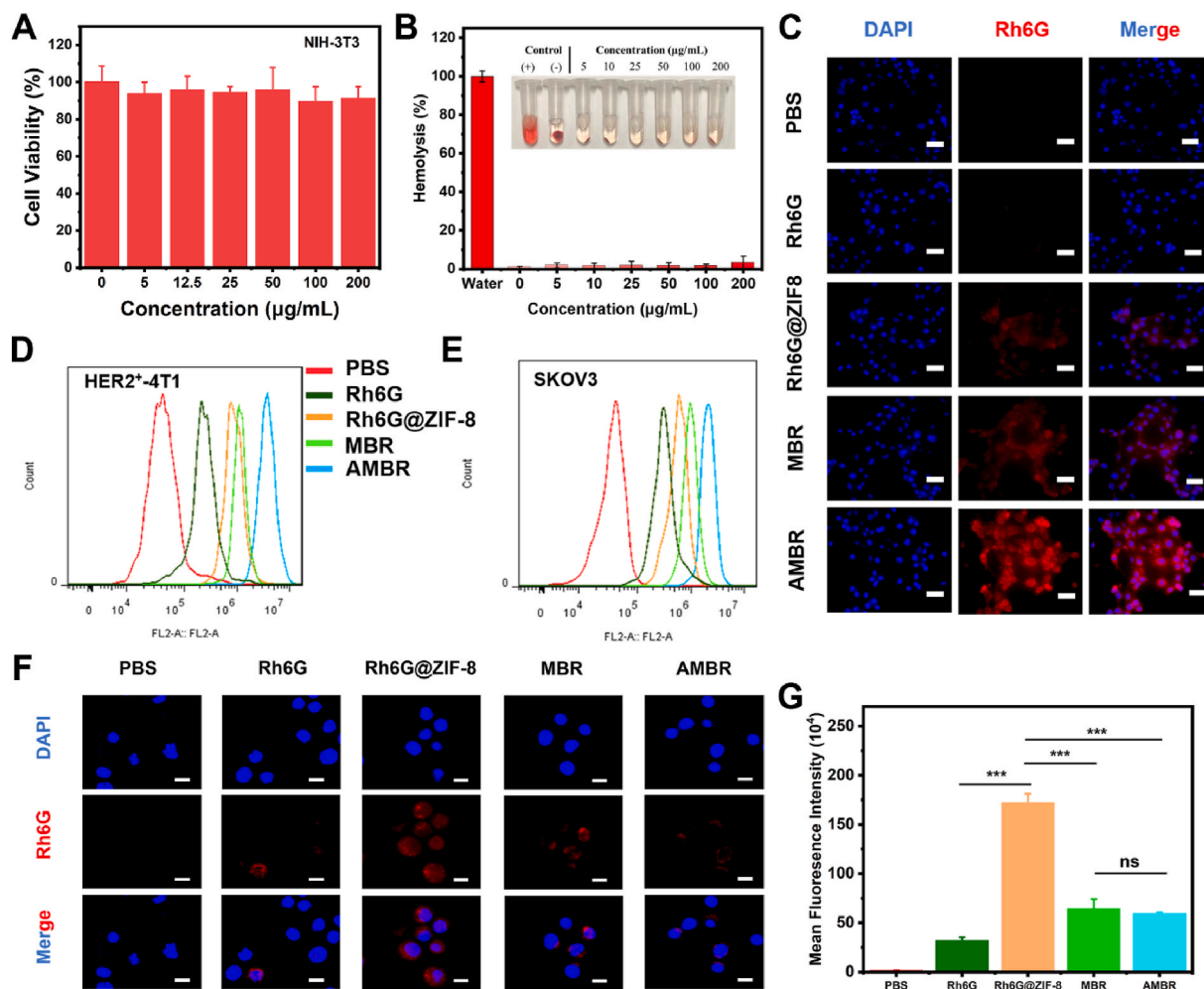


**Fig. 3.** Cellular uptake and immune escape of AMBP NPs. A) Cell Viability of AMBP NPs on NIH-3T3 cell lines. B) Hemolysis analysis of red blood cells after incubation with AMBP NPs at different concentrations. C) CLSM results of HER2<sup>+</sup>-4T1 cells incubated with different format nanomaterials to verify their cellular uptake performance. NPs were labeled with Rh6G (Red) and nuclei were stained with DAPI (Blue). Flow cytometry assay of D) HER2<sup>+</sup>-4T1 cells and E) SKOV3 cells incubated with different formats to verify their cellular uptake behavior. F) CLSM results and of macrophages incubated with different formats to demonstrate their immune escape ability of macrophages. NPs were labeled with Rh6G (Red) and nuclei were stained with DAPI (Blue). ZIF-8 enhanced the uptake of Rh6G by macrophages whereas the macrophage coating reduced the uptake of Rh6G@ZIF-8 by macrophages after each group co-culturing with macrophages, respectively. G) The Mean fluorescence intensity by flow cytometry analysis to show their immune escape behaviors. Results are presented as means  $\pm$  SD. \*\*\* $P < 0.001$ , n.s., not significant,  $P > 0.05$ .

in the binding sites for both proteins showed correlated motions when the system reached the equilibrium state after 8 ns, indicating that the anti-HER2 and HER2 binding systems exhibited an increase in correlated movements. Overall, the simulation results show that the HER2 identification mechanism was not affected by our modified macrophage method.

### 3.2. Synthesis and characterization of the AMBP nanoplatform

Considering the spatiotemporally controlled photothermal therapy [19], IR820 fluorescent dyes with good imaging performance and excellent biocompatibility were used to verify our concept. AMBP nanoplatform were built using a two-step process similar to our previous approach. First, a one-pot synthesis process was used to create a defect self-assembly structure containing the IR820@ZIF-8 nanoparticles to shield the IR820 molecule from photobleaching (Fig. 2A) [20]. The images obtained using transmission electron microscopy (TEM) (Fig. 2B) further show that the nanoparticles had a well-dispersed, spherical structure with a size of approximately 70 nm. As shown in the 2C's dynamic light scattering (DLS) profiles, the nanoparticles had a hydrodynamic size of 90 nm. The hydration of the nanoparticles in the

solution causes the differences between the DLS and SEM results. IR820@ZIF-8 was effectively loaded within ZIF-8 because its ultraviolet–visible (UV–Vis) absorption peak of IR820@ZIF-8 was raised at 820 nm (Fig. 2D). The basic structure of IR820@ZIF-8 was confirmed using an X-ray diffraction pattern [26]. Fig. 2E shows that characteristic diffraction peaks at approximately  $2\theta = 7.7^\circ$ ,  $13.1^\circ$ , and  $18.5^\circ$  correspond to ZIF-8, indicating that the encapsulation of IR820 would not affect the crystal structure. Moreover, IR820@ZIF-8 nanoparticles exhibited a surface charge of approximately +20 mV (Fig. 2F), and this distinctively positive surface charge facilitates the subsequent membrane coating.

As previously mentioned, blood circulation time and tumor accumulation in solid BC must be enhanced [27]. Modified macrophage membranes were extracted for developing AMBP to conceal the phototherapeutic nanoplatform IR820@ZIF-8 (Fig. 2A). According to the DLS data, the particle size increased from 90 to 130 nm. Modification with a biomimetic macrophage containing many negatively charged amino acids was confirmed when the zeta potential changed from +20 mV for IR820@ZIF-8 to  $-10$  mV. Additionally, the TEM and SEM images of the AMBP NPs revealed a fuzzy layer (Fig. 2B and Fig. S4). To confirm the composition of AMBP NPs, sodium dodecyl sulfate-polyacrylamide gel

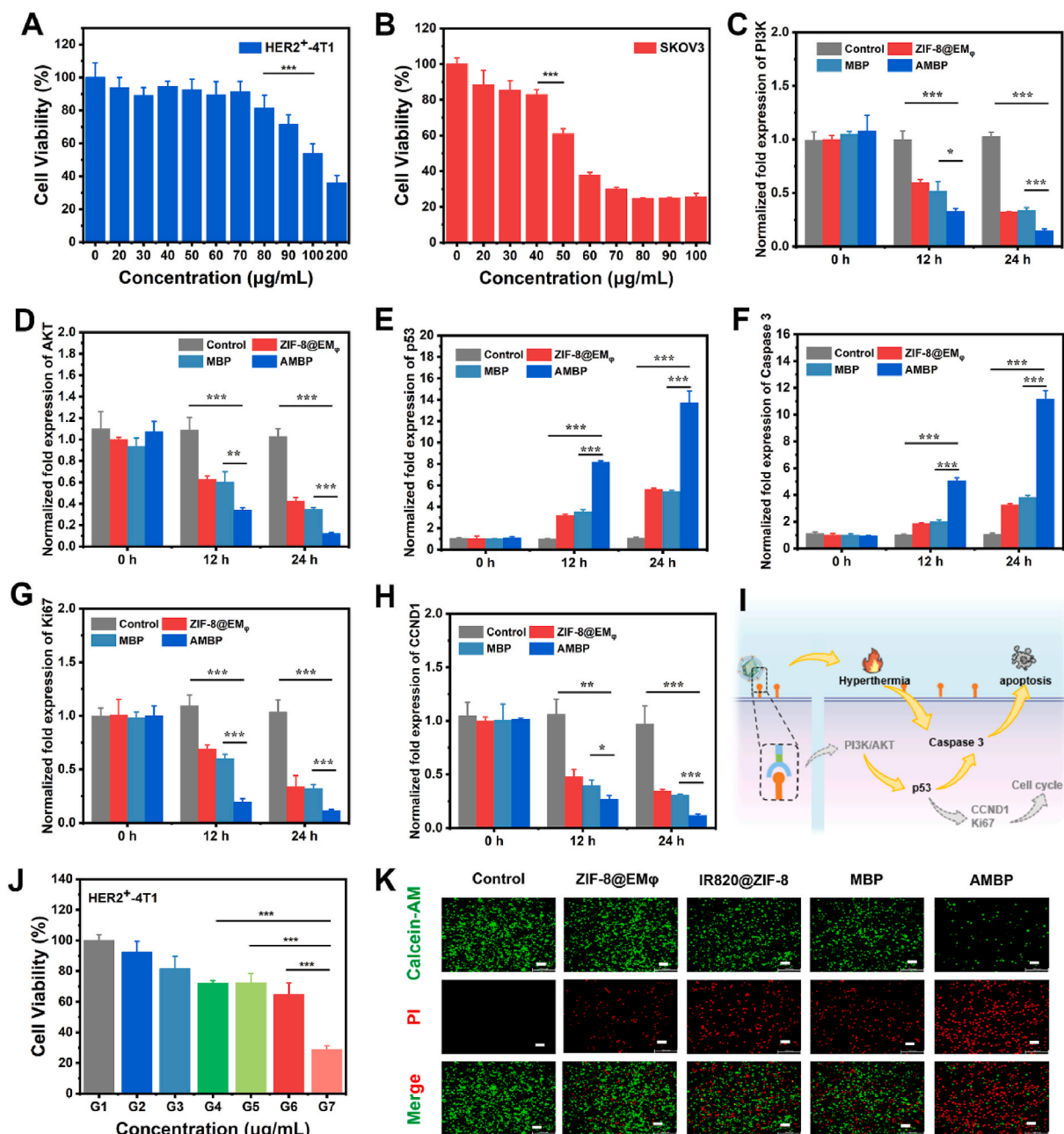


**Fig. 4.** *In vitro* Anti-tumor Effect of AMBP NPs. A) Cell viability of AMBP NPs on HER2<sup>+</sup>-4T1 cell lines. B) Cell viability of AMBP NPs on SKOV3 cell lines. qRT-PCR assays of C) PI3K mRNA, D) AKT mRNA, E) p53 mRNA, F) Caspase 3 mRNA, G) Ki67 mRNA, and H) CCND-1 mRNA in HER2<sup>+</sup>-4T1 cells with different treatments. I) Schematic illustration shows their bio-photothermal synergistic therapy mechanism. J) Cell viability of nanomaterials on HER2<sup>+</sup>-4T1 cell lines to show their combined therapeutic effect. (G1: PBS, G2: Laser, G3: IR820, G4: ZIF-8@EM $\phi$ , G5: IR820@ZIF-8, G6: MBP NPs, G7: AMBP NPs). K) CLSM images of HER2<sup>+</sup>-4T1 cells stained with calcein AM (green, live cells) and propidium iodide (red, dead cells) after different treatments. Scale bar = 50  $\mu\text{m}$ . Data are expressed as the mean  $\pm$  s.d. (\* $P$  < 0.05, \*\* $P$  < 0.01, and \*\*\* $P$  < 0.001).

electrophoresis (SDS-PAGE) was performed. The SDS-PAGE results demonstrated that macrophage membrane proteins were reserved in large quantities in the AMBP group [28], further supporting that the membranes of macrophages were coated (Fig. 2G). TEM showed a core/shell structure of the AMBP NPs, with a size increase of approximately 15 nm. All the aforementioned findings demonstrate that we successfully created a biomimetic nanoplatform based on phototherapeutic IR820@ZIF-8 nanoparticles and membrane-modified macrophages.

We then evaluated the photothermal behavior of the nanomaterials with and without the macrophage coating. Free IR820 solution exhibits a dose-dependent photothermal response when exposed to an NIR laser

(Fig. S5), and the photothermal conversion efficiency is 36.5%. Notably, the extreme photobleaching effect causes the temperature to decrease as the exposure time increased [20]. However, with the protection of the ZIF-8 shell, IR820@ZIF-8 (Fig. S6), and AMBP NPs (Fig. 2H) showed similar temperatures when encapsulated with the same concentration of IR820 dye. For instance, the level of temperature rise was flexibly controlled in the range of 40–60  $^{\circ}\text{C}$  by adjusting the concentration of AMBP NPs from 10 to 100  $\mu\text{g mL}^{-1}$  (Fig. 2H) or changing the power density from 0.25 to 2  $\text{W cm}^{-2}$  (Fig. 2I). Furthermore, the photothermal conversion efficiency of MBP and AMBP was 42.7, and 41.6%, respectively (Fig. S7). Finally, several exposures to NIR light (808 nm) were used to evaluate the photostability of AMBP.

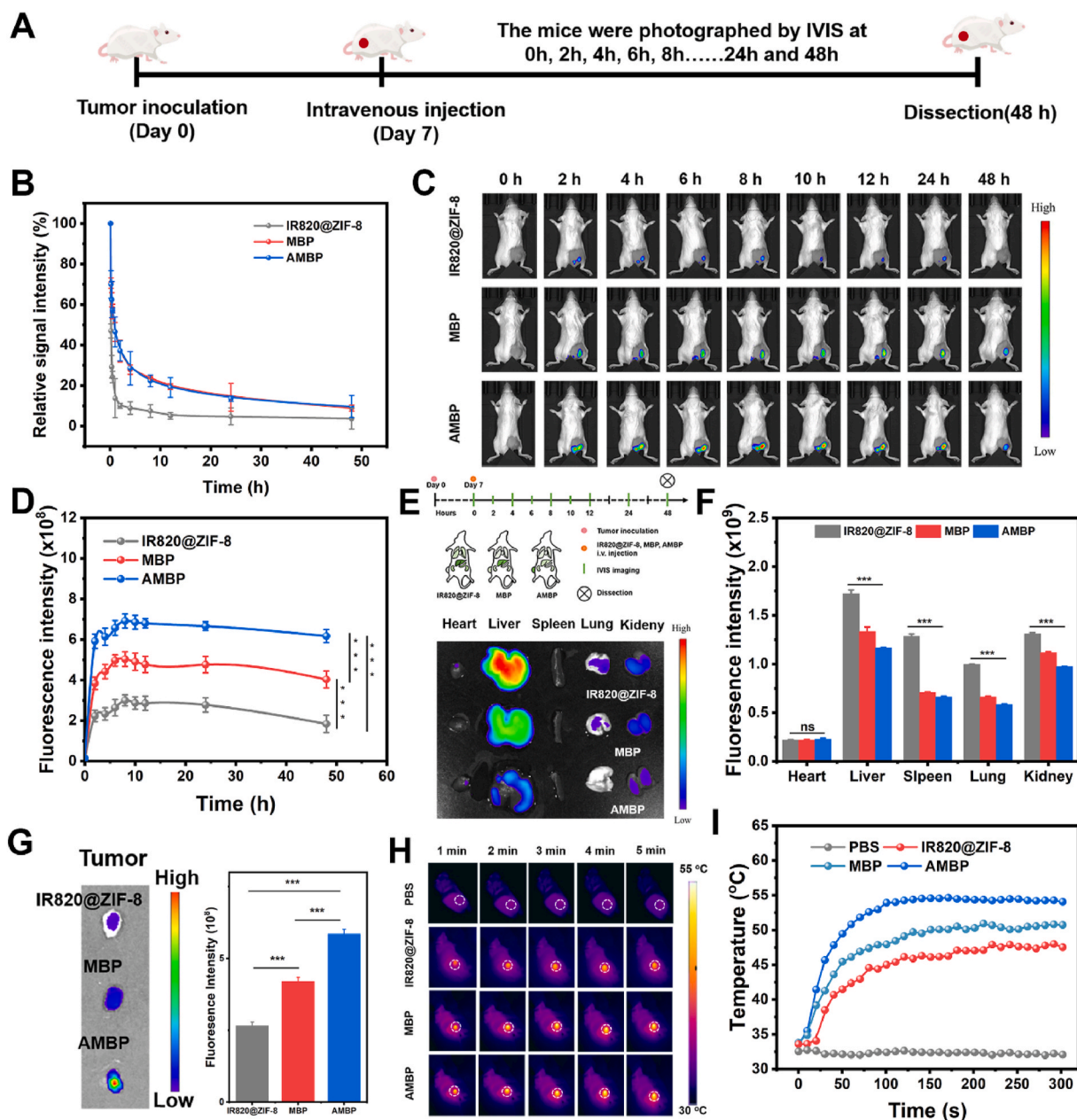


**Fig. 5.** Pharmacokinetics and biodistribution of AMBP NPs *in vivo*. A) Schematic illustration shows their protocols. B) Pharmacokinetic profiles of IR820@ZIF-8, MBP, and AMBP NPs in normal BALB/c mice (Ex: 710 nm, Em: 820 nm). C) *In vivo* fluorescence imaging of IR820@ZIF-8, MBP and AMBP NPs in HER2<sup>+</sup>-4T1 tumor-bearing mice (Ex: 710 nm, Em: 820 nm). D) The Fluorescence intensity within the tumor region after different treatments. E) *Ex vivo* fluorescence images of major organs (heart, liver, spleen, lung, kidney) at 8 h post-injection. F) Biodistribution of IR820@ZIF-8, MBP and AMBP NPs in HER2<sup>+</sup>-4T1 tumor-bearing mice at 8 h post-injection. G) *Ex vivo* fluorescence images of tumors under different treatments. H) Infrared thermal images of PBS, IR820@ZIF-8, MBP and AMBP NPs upon 808 nm laser (1W cm<sup>-2</sup>) irradiation for 5 min. I) The Temperature elevation curves of different treatments. Results are presented as means  $\pm$  SD. \*\*\* $P < 0.001$ , n.s., not significant,  $P > 0.05$ .

The good photostability and anti-photobleaching of cyanine molecules were caused by the ZIF-8 structure [20], as shown by the fact that the peak temperature of AMBP remained stable under five NIR irradiations, as opposed to the rapid decay of the free IR820 group (Fig. 2J). Supporting the ability of ZIF-8 shell to shield IR820 dyes from photobleaching is the typical absorption spectrum shown in Fig. 2K, which continued to show a modest decrease after five exposures.

### 3.3. Cellular uptake and immune escape of the AMBP nanoplatform

Cytotoxicity of the AMBP nanoplatform in mouse embryo NIH-3T3 cells (Fig. 3A) and human embryonic kidney 293T cells (Fig. S8) was

assessed using a standard MTT assay [29]. Even at a concentration of 200 g mL<sup>-1</sup>, cell viability was essentially identical to that of the control group, demonstrating that AMBP had little cytotoxicity. *In vivo* hemolysis results in a considerable decrease in red blood cells, impairing their ability to carry oxygen, which could damage organs or tissues and result in toxicity in the body [30]. A hemolytic test (Fig. 3B) confirmed that even at high concentrations of up to 200 g mL<sup>-1</sup>, AMBP NPs did not harm red blood cells. This phenomenon is because AMBP has good biocompatibility owing to its nontoxic components.

Encouraged by the biocompatibility results, cellular uptake tests were conducted by incubating HER2<sup>+</sup>-4T1 cells with various nanoparticle formations at 37 °C. Rh6G dye (Em: 530 nm, Ex: 556 nm) was

used to replace IR820 for the confocal laser scanning microscopy (CLSM) experiments to obtain fluorescence signals within the NIR range. Fig. S9 depicts the fundamental characteristics of Rh6G@ZIF-8, which are similar to IR820@ZIF-8 in size and morphology. The CLSM images in Fig. 3C show that a negligible fluorescence signal of the free Rh6G group was obtained, and the fluorescence brightness of the Rh6G@ZIF-8 and Rh6G@ZIF-8@M<sub>φ</sub> (MBR) groups was slightly improved owing to the endocytosis of the HER2<sup>+</sup>-4T1 cancer cells. However, the red fluorescence signal of the Rh6G@ZIF-8@EM (AMBR) group was noticeably improved, caused by the successful interaction of the anti-HER2 protein domain with HER2 and increased endocytosis efficiency. The cellular uptake of AMBR was quantitatively analyzed using flow cytometry. Fig. 3D shows that the AMBR group had the highest levels of cellular uptake. To further confirm the cellular uptake behavior of HER2, we used a high expression of HER2, excluding the interference of cell lines, especially the SKOV3 cell line. A similar red fluorescence signal confirmed that AMBR was phagocytosed by the SKOV3 cells (Figs. S10 and 3E). In addition, RAW 264.7 cells (a mouse macrophage cell line) confirmed the immune escape behavior of AMBR (Fig. 3F and G). After co-incubation with macrophages and different nanoparticle formations, the Rh6G@ZIF-8 group displayed a higher red fluorescence intensity than those treated with free Rh6G, MBR, and AMBR. Therefore, we concluded that AMBR could be effectively phagocytosed by HER2<sup>+</sup> cancer cells and that the coating of macrophages or anti-HER2 EM would endow the nanoparticles with immune escape ability to reduce macrophage cellular uptake [31].

### 3.4. Enhanced *in vitro* anti-tumor effect of the AMBP nanopatform

After confirming AMBP's photothermal abilities and immune evasion capacity, we then investigated its *in vitro* anti-tumor effect. First, several cell lines were used to study anti-tumor activities. Fig. 4A illustrates how AMBP significantly killed HER2<sup>+</sup>-4T1 cell lines while remaining biocompatible with NIH-3T3 and 293T cell lines, suggesting that the anti-HER2 expressed macrophages play a key role in the cytotoxic action of AMBP. Further testing of their anti-tumor properties was performed using SKOV-3 cell lines (high expression of HER2) and normal 4T1 cell lines (without HER2 expression, Figs. S11 and S12) to confirm their specific cytotoxicity from HER2-related biotherapy [3]. Fig. 4B shows that 61.3 % and 23.7 % of the cells survived in solutions containing 50 and 100 g mL<sup>-1</sup> AMBP, respectively. Studies have indicated that the armed anti-HER2 antibody domain has a favorable effect on cell survival. We conducted mechanistic studies on the pathway linked to the HER2 target to elucidate the mechanism by which coating IR820@ZIF-8 with a membrane-armed anti-HER2 antibody promotes cell cytotoxicity. In general, the phosphatidylinositol 3-kinase/AKT/mammalian target of rapamycin (PI3K/AKT/mTOR) pathway is a critical intracellular signaling pathway that drives cellular development and survival, and hyperactivation of this pathway was linked to cancer in HER2<sup>+</sup> cell lines [32]. Anti-HER2 antibody-enhanced membrane-camouflaged nanoparticles targeted and detected HER2 proteins while inducing apoptosis in HER2<sup>+</sup> cells. We validated the mRNA expression levels of PI3K and AKT, the primary downstream effector enzymes of this pathway. The qPCR findings for PI3K (Fig. 4C) and AKT (Fig. 4D) showed a downregulation pattern with incubation time, attributed to the suppression of the HER2 target negative regulatory PI3K/AKT pathway. Furthermore, inhibiting the HER2 target influences the apoptosis-related p53 and the downstream indicator Caspase-3 of the PI3K/AKT pathway. We examined the mRNA expression levels of p53 and Caspase-3. The negative regulatory connection between downstream indicators (p53 and Caspase-3) and HER2 suppression suggests that AMBP-treated HER2<sup>+</sup>-4T1 cancer cells are susceptible to HER2-induced apoptosis (Fig. 4E and F). However, when treated with AMBP, an armed anti-HER2 antibody membrane efficiently targets and blocks the HER2 protein while inhibiting cell proliferation-associated indicators. The mRNA levels of Ki 67 (Fig. 4G)

and Cyclin D1 (Fig. 4H) were also downregulated. Further evidence that the PI3K/AKT pathway is one of the key underlying mechanisms causing cytotoxicity in the armed anti-HER2 antibody membrane (Fig. 4I) is obtained from the observation of the same mRNA expression patterns in MDA-MB-453 (Fig. S15) and SKOV3 cell lines (Fig. S16).

These results motivated us to investigate whether photothermal effects contribute to the enhanced cytotoxicity of biotherapeutics. Initially, we tested the photothermal effect *in vitro* and discovered that free IR820 (G3) and IR820@ZIF-8 (G5) exhibited low cytotoxicity (Fig. 4J). However, with the combination of the photothermal effect and anti-HER2 induced biotherapeutics (G7), cell viability was reduced substantially to 25 %. In contrast, cell survival of the normal macrophage modification group (G6) exhibited no noticeable change, indicating that the armed anti-HER2 antibody membrane caused cytotoxicity. Furthermore, the photothermal impact increases the activity of apoptosis-associated pathways. Under NIR irradiation, p53 and Caspase-3 expression were strongly upregulated in both combination treatment groups (MBP and AMBP; Fig. 4E and F). Longer treatment duration may be associated with increased mRNA expression. Furthermore, CLSM images of Calcein AM-and propidium iodide (PI)-stained HER2<sup>+</sup>-4T1 cells demonstrated that AMBP has a strong therapeutic effect, and cells in this group have prominent red fluorescence signals, which reflect dead cells. However, the AMB, IR820@ZIF-8, and MBP groups displayed much higher green signals than AMBP-treated cells (Fig. 4K). Finally, all the aforementioned data were also validated in the human HER2-positive MDA-MB-453 cell lines (Figs. S13–S15) and SKOV3 cell line (Figs. S16–S18).

### 3.5. Pharmacokinetics and biodistribution of AMBP *in vivo*

Because of the excellent *in vitro* cell killing performance, we aimed to explore the anti-tumor effects of AMBP *in vivo*. Before conducting this experiment, AMBP was administered to normal BALB/c and HER2<sup>+</sup>-4T1 tumor-bearing mice via tail vein injection (Fig. 5A). The pharmacokinetics results in Fig. 5B show that MBP and AMBP share almost the same metabolic behaviors, with a half-life (5.89 h ± 0.92 h and 5.31 h ± 0.71 h), indicating that the engineered anti-HER2 has negligible influence on its prolonged blood circulation time. However, without a macrophage membrane coating, IR820@ZIF-8 was rapidly eliminated from the blood owing to its high immunogenicity. To intuitively observe the biodistribution of AMBP and its accumulation in tumors, we developed HER2<sup>+</sup>-4T1 tumor-bearing mice. As shown in Fig. 5C, mice treated with IR820@ZIF-8 demonstrated a low fluorescent signal within the tumor region and rapid metabolism from the body 24 h post injection, owing to rapid uptake by the reticuloendothelial system (RES) [33]. However, with the modification of EM, the AMBP group showed a greater residual concentration than that of the IR820@ZIF-8 group at 48 h post-injection (Fig. 5C), with 2.3- and 7.9-fold higher concentrations than those of the IR820@ZIF-8 group and skin background signals, respectively. Furthermore, considerable fluorescence intensities were observed at the tumor site (Fig. 5C and D) in the MBP- and AMBP-treated animals. AMBP fluorescence signals at the tumor location were detected after 2 h and steadily increased until they reached their maximum at 8 h post-injection. Next, the biodistribution of AMBP NPs was examined by *ex vivo* fluorescence imaging of key organs and tumors 8 h after injection. The fluorescence intensities of the liver and kidneys in IR820@ZIF-8-treated animals were significantly higher than those of normal macrophages (Fig. 5E and F). In general, nanomaterials (sized > 100 nm) are usually phagocytosed by mononuclear macrophage, leading to a shorter half-life pharmacokinetics behaviors [31]. However, the extended half-life of MBP, and AMBP indicated that the biological membrane-camouflaged may contribute to the escape from phagocytes in the blood. Moreover, the different uptake behaviors of nanoparticles by macrophage in Fig. 3F also supported the escape behaviors from phagocytes. Therefore, these results indicated that macrophages-camouflaged nanoparticles could escape from phagocytes

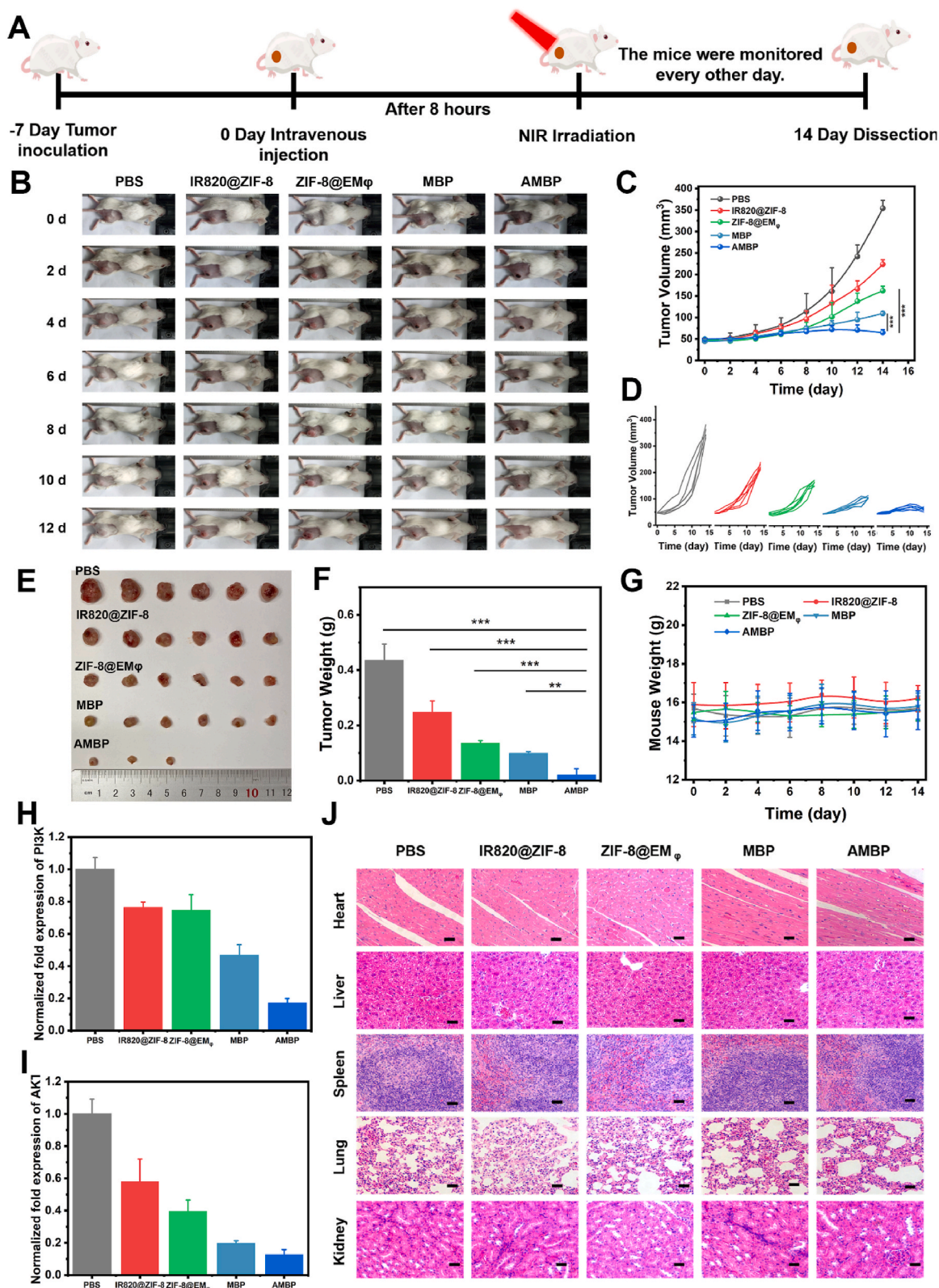


**Fig. 6.** Tumor therapy of AMBP NPs *in vivo*. A) Schematic illustration shows their protocols. B) Images of HER2<sup>+</sup>-4T1 tumor-bearing mice under different treatments (i.e. PBS, control group, IR820@ZIF-8: phototherapeutic group, ZIF-8@EM<sub>φ</sub>: biotherapeutic group, MBP NPs, AMBP NPs, photothermal therapy and biotherapy). C) The Average tumor volume curves of mice after various treatments. D) Individual tumor growth curves of mice after various treatments. E) Images of HER2<sup>+</sup>-4T1 tumor-bearing mice under different treatments. F) Tumor weight of HER2<sup>+</sup>-4T1 tumor-bearing mice with different treatments. G) The Mice weight curves. qRT-PCR assays of H) PI3K mRNA, I) AKT mRNA in HER2<sup>+</sup>-4T1 tumor-bearing mice. J) H&E staining of major mice organs. Data are expressed as the mean ± s.d. (\*\**P* < 0.01, and \*\*\**P* < 0.001).

in the blood. The *ex vivo* fluorescence of tumors in the AMBP-treated mice was substantially brighter than that in the IR820@ZIF-8- and MBP-treated animals (Fig. 5G). The increased accumulation of AMBP in tumors can be ascribed to its long blood circulation and HER2-targeting capacity. Overall, the improved tumor fluorescence imaging and tumor accumulation results show that our synthesized AMBP systems have a high potential for anti-tumor applications *in vivo*.

### 3.6. Tumor therapy *in vivo*

The combined *in vivo* anti-tumor efficacy of phototherapy/biotherapy was estimated in breast tumor mouse models established by inoculating HER2<sup>+</sup>-4T1 cells. First, photoradiation was implemented 8 h post-injection to examine the *in vivo* therapeutic efficacy. IR820@ZIF-8, MBP, and AMBP were injected *i.v.* before photoradiation (Fig. 5H). When the mice were irradiated with the 808 nm laser (1 W cm<sup>-2</sup> and 5 min), the temperature of the tumor region containing MBP and AMBP increased rapidly from 30 to 54 °C (Fig. 5I), and negligible change in temperature was observed in the PBS group. Moreover, the MBP and IR820@ZIF-8 groups showed an insufficient elevated temperature (17 °C and 14 °C) due to non-specific tumor targeting.

For assessing the synergistic photothermal/biotherapy *in vivo*, HER2<sup>+</sup>-4T1 tumor-bearing BALB/c mice were randomly separated into five groups (n = 6), and different formulations of nanoparticles were injected from the tail veins (Fig. 6A). Notably, ZIF-8@EM<sub>p</sub> and MBP alone can delay tumor growth but failed to achieve durable control of tumor progression in all treated mice, indicating that the biotherapy and the photothermal therapy as a monotherapy are inadequate for anti-tumor effects *in vivo* (Fig. 6B–F). However, the AMBP treatment resulted in the total elimination of the tumors in three of the six mice (Fig. 6B–F). The *ex vivo* sizes and weights of the tumors further validate their anti-tumor activity (Fig. 6E and F). Furthermore, the AMBP therapy had no influence on body weight, indicating that the AMBP nanoplatform was relatively safe *in vivo* (Fig. 6G). The PI3K/AKT pathway and its downstream indicators were assessed using qPCR to elucidate the precise mechanism of the *in vivo* anti-tumor activities. The *in vivo* results shown in Fig. 6H and I are consistent with the *in vitro* cell experiment results (Fig. 4C–K). Caspase-3 and p53 were upregulated in.

armed anti-HER2 antibody membrane-treated mice, and Ki67 and Cyclin D1 were downregulated (Fig. S19). All groups were sacrificed under the Animal Care Act on the 14th day after treatment if there was no significant tumor burden. The primary organs (i.e. heart, liver, spleen, lungs, and kidneys) were removed and stained with hematoxylin and eosin (H&E). As illustrated in Fig. 6J, no visible tissue damage was observed in the H&E-stained images, confirming high *in vivo* biocompatibility. Overall, the *in vivo* anti-tumor findings were consistent with the *in vitro* cytotoxicity, indicating that the AMBP nanoplatform may be used as an alternative strategy to improve the therapeutic efficacy of solid BC.

## 4. Conclusion

In conclusion, we developed an AMBP nanoplatform with HER2 targeting, high circulation properties, and effective photothermal effects for HER2<sup>+</sup> BC tumor elimination. IR820 molecules were loaded into ZIF-8 to resist photobleaching using a coordination connection between the metal ions and IR820 molecules. Meanwhile, the anti-HER2 antibody was expressed in engineered macrophages using the transmembrane expression technique. Homology modeling methods support that the expressed anti-HER2 antibody can effectively recognize the HER2 receptor. Additionally, the as-prepared AMBP may effectively target and concentrate inside the tumor site owing to the interaction between the anti-HER produced on macrophages and the HER2 protein in tumor cells. Moreover, our results have been also established that antibody-dependent cell-mediated cytotoxicity can also be induced in HER2<sup>+</sup>

BC cells by AMBP. Notably, based on the high tumor accumulation, AMBP show an enhanced bio-photothermal synergistic therapy for HER2<sup>+</sup> malignancies. In conclusion, our research opens a new paradigm for antibody-specific macrophage, and it is expected that these characteristics will have substantial clinical translation potential for BC treatment.

### CRedit authorship contribution statement

**Peng Yang:** Writing – original draft, Investigation, Formal analysis. **Fuyu Du:** Writing – original draft, Software, Data curation. **Weijie Zhang:** Investigation. **Weijing Liu:** Formal analysis. **Zixuan Ye:** Data curation. **Hongyu Fan:** Formal analysis. **Jie Yu:** Software. **Karen M. von Deneen:** Writing – original draft. **Zhongliang Wang:** Writing – review & editing, Project administration, Funding acquisition, Conceptualization. **Pengbo Ning:** Writing – review & editing, Validation, Supervision, Project administration, Investigation, Funding acquisition, Formal analysis, Data curation, Conceptualization.

### Declaration of competing interest

All authors declare that they have no conflicts of interest and no competing interest.

### Data availability

No data was used for the research described in the article.

### Acknowledgements

P. Yang and F. Du contributed equally to this work. This work was supported by the National Natural Science Foundation of China (32071406, 82272159, and 32371433), the Original Exploration Project of National Natural Science Foundation of China (82350124), Key Research and Development Projects of Shaanxi Province (2023-ZDLSF-18), the Dual-chain Integration Special Program of Qinchuangyuan Construction (23LLRH0070), Innovation Capability Support Program of Shaanxi (2022TD-52), Youth Innovation Team of Shaanxi Universities, the Key R & D program of Xianyang City (2021ZDYF-SF-0023, L2023-ZDYF-SF-004), Xi'an Science and Technology Planning project (21NYFF0013) for their financial support.

### Appendix A. Supplementary data

Supplementary data to this article can be found online at <https://doi.org/10.1016/j.mtbio.2024.101095>.

### References

- [1] C. Criscitiello, S. Morganti, G. Curigliano, J. Hematol. Oncol. 14 (2021) 20.
- [2] R.L. Siegel, K.D. Miller, N.S. Wagle, A. Jemal, CA A Cancer J. Clin. 73 (2023) 17.
- [3] H. Wang, D. Jia, D. Yuan, X. Yin, F. Yuan, F. Wang, W. Shi, H. Li, L.M. Zhu, Q. Fan, J. Nanobiotechnol. 19 (2021) 138.
- [4] A. Juan, F.J. Cimas, I. Bravo, A. Pandiella, A. Ocana, C. Alonso-Moreno, Int. J. Mol. Sci. 21 (2020) 6018.
- [5] Y.Z. Liu, X.Y. Ran, D.H. Zhou, H. Zhang, Y.J. Chen, J.X. Xu, S.Y. Chen, Q.Q. Kong, X.Q. Yu, K. Li, Adv. Funct. Mater. (2023) 2311365.
- [6] Y. Xiong, Y. Rao, J. Hu, Z. Luo, C. Chen, Adv. Mater. (2023) 2305140.
- [7] Y. Zou, M. Li, T. Xiong, X. Zhao, J. Du, J. Fan, X. Peng, Small 16 (2020) 1907677.
- [8] A.R. Rastinehad, H. Anastos, E. Wajswol, J.S. Winoker, J.P. Sfakianos, S. K. Doppalapudi, M.R. Carrick, C.J. Knauer, B. Taouli, S.C. Lewis, A.K. Tewari, J. A. Schwartz, S.E. Canfield, A.K. George, J.L. West, N.J. Halas, Proc. Natl. Acad. Sci. U.S.A. 116 (2019) 18590.
- [9] L. Cheng, C. Wang, L. Feng, K. Yang, Z. Liu, Chem. Rev. 114 (2014) 10869.
- [10] S.G. Alamdari, M. Amini, N. Jalilzadeh, B. Baradaran, R. Mohammadzadeh, A. Mokhtarzadeh, F. Oroojalian, J. Contr. Release 349 (2022) 269.
- [11] D. Huang, Q. Wang, Y. Cao, H. Yang, M. Li, F. Wu, Y. Zhang, G. Chen, Q. Wang, ACS Nano 17 (2023) 5033.
- [12] Y. Liu, J. Luo, Y. Liu, W. Liu, G. Yu, Y. Huang, Y. Yang, X. Chen, T. Chen, ACS Cent. Sci. 8 (2022) 1336.
- [13] C.M. Hu, R.H. Fang, J. Copp, B.T. Luk, L. Zhang, Nat. Nanotechnol. 8 (2013) 336.

- [14] S. Thamphiwatana, P. Angsantikul, T. Escajadillo, Q. Zhang, J. Olson, B.T. Luk, S. Zhang, R.H. Fang, W. Gao, V. Nizet, L. Zhang, *Proc. Natl. Acad. Sci. U.S.A.* 114 (2017) 11488.
- [15] Q. Zhang, D. Dehaini, Y. Zhang, J. Zhou, X. Chen, L. Zhang, R.H. Fang, W. Gao, L. Zhang, *Nat. Nanotechnol.* 13 (2018) 1182.
- [16] G. Wu, J. Zhang, Q. Zhao, W. Zhuang, J. Ding, C. Zhang, H. Gao, D.W. Pang, K. Pu, H.Y. Xie, *Angew. Chem. Int. Ed.* 59 (2020) 4068.
- [17] Z. Rao, C. Lu, H. Fan, F. Du, Y. Zhu, Y. Xia, Z. Wang, P. Ning, *Adv. Healthcare Mater.* 12 (2023) 2203356.
- [18] A. Ruiz-Saenz, C. Dreyer, M.R. Campbell, V. Steri, N. Gulizia, M.M. Moasser, *Cancer Res.* 78 (2018) 3645.
- [19] P. Yang, Y. Tian, Y. Men, R. Guo, H. Peng, Q. Jiang, W. Yang, *ACS Appl. Mater. Interfaces* 10 (2018) 42039.
- [20] P. Yang, Y. Men, Y. Tian, Y. Cao, L. Zhang, X. Yao, W. Yang, *ACS Appl. Mater. Interfaces* 11 (2019) 11209.
- [21] X. Zhang, B. Wang, N. Zhao, Z. Tian, Y. Dai, Y. Nie, J. Tian, Z. Wang, X. Chen, *Theranostics* 7 (2017) 3794.
- [22] A. Waterhouse, M. Bertoni, S. Bienert, G. Studer, G. Tauriello, R. Gumienny, F. T. Heer, T.A.P. de Beer, C. Rempfer, L. Bordoli, R. Lepore, T. Schwede, *Nucleic Acids Res.* 46 (2018) 296.
- [23] Y. Yan, H. Tao, J. He, S.-Y. Huang, *Nat. Protoc.* 15 (2020) 1829.
- [24] J. Wu, J. Zhang, H.X. Zhang, *Langmuir* 38 (2022) 10690.
- [25] S.A. Poveda Cuevas, F.L. Barroso da Silva, C. Etchebest, *J. Chem. Inf. Model.* 63 (2023) 1386.
- [26] Q. Zhao, Z. Gong, Z. Li, J. Wang, J. Zhang, Z. Zhao, P. Zhang, S. Zheng, R.J. Miron, Q. Yuan, Y. Zhang, *Adv. Mater.* 33 (2021) 2100616.
- [27] T.H. Shin, E.S. Sung, Y.J. Kim, K.S. Kim, S.H. Kim, S.K. Kim, Y.D. Lee, Y.S. Kim, *Mol. Cancer Therapeut.* 13 (2014) 651.
- [28] M. Hou, Y. Wei, Z. Zhao, W. Han, R. Zhou, Y. Zhou, Y. Zheng, L. Yin, *Adv. Mater.* 32 (2022) 2108817.
- [29] Z. Chen, W. Liu, Z. Yang, Y. Luo, C. Qiao, A. Xie, Q. Jia, P. Yang, Z. Wang, R. Zhang, *Theranostics* 13 (2023) 1571.
- [30] J. Zhang, B. Gao, B. Ye, Z. Sun, Z. Qian, L. Yu, Y. Bi, L. Ma, Y. Ding, Y. Du, W. Wang, Z. Mao, *Adv. Mater.* 35 (2023) 2208571.
- [31] Y. Xia, L. Rao, H. Yao, Z. Wang, P. Ning, X. Chen, *Adv. Mater.* 32 (2020) 2002054.
- [32] L.R. Mangiapane, A. Nicotra, A. Turdo, M. Gaggianesi, P. Bianca, S. Di Franco, D. S. Sardina, V. Veschi, M. Signore, S. Beyes, L. Fagnocchi, M.E. Fiori, M. R. Bongiorno, M. Lo Iacono, I. Pillitteri, G. Ganduscio, G. Gulotta, J.P. Medema, A. Zippo, M. Todaro, R. De Maria, G. Stassi, *Gut* 71 (2022) 119.
- [33] L. Yan, F. Zhao, J. Wang, Y. Zu, Z. Gu, Y. Zhao, *Adv. Mater.* 31 (2019) 1805391.